The Astrophysical Journal, 962:89 (10pp), 2024 February 10 https://doi.org/10.3847/1538-4357/ad132e

Small-amplitude Compressible Magnetohydrodynamic Turbulence Modulated by Collisionless Damping in Earth's Magnetosheath: Observation Matches Theory

Siqi Zhao[1,2], Huirong Yan[1,2,6], Terry Z. Liu[3], Ka Ho Yuen[4], and Mijie Shi[5]
[1] Deutsches Elektronen Synchrotron DESY, Platanenallee 6, D-15738, Zeuthen, Germany; huirong.yan@desy.de
[2] Institut für Physik und Astronomie, Universität Potsdam, D-14476, Potsdam, Germany
[3] Department of Earth, Planetary, and Space Sciences, University of California, Los Angeles, CA 90024, USA; terryliuzixu@ucla.edu
[4] Theoretical Division, Los Alamos National Laboratory, Los Alamos, NM 87545, USA
[5] Shandong Key Laboratory of Optical Astronomy and Solar-Terrestrial Environment, Institute of Space Sciences, 264209, Shandong University, Weihai, People's Republic of China
Received 2023 October 16; revised 2023 December 1; accepted 2023 December 5; published 2024 February 8

Abstract

Plasma turbulence is a ubiquitous dynamical process that transfers energy across many spatial and temporal scales and affects energetic particle transport. Recent advances in the understanding of compressible magnetohydrodynamic (MHD) turbulence demonstrate the important role of damping in shaping energy distributions on small scales, yet its observational evidence is still lacking. This study provides the first observational evidence of substantial collisionless damping (CD) modulation on the small-amplitude compressible MHD turbulence cascade in Earth's magnetosheath using four Cluster spacecraft. Based on an improved compressible MHD decomposition algorithm, turbulence is decomposed into three eigenmodes: incompressible Alfvén modes and compressible slow and fast (magnetosonic) modes. Our observations demonstrate that CD enhances the anisotropy of compressible MHD modes because CD has a strong dependence on wave propagation angle. The wavenumber distributions of slow modes are mainly stretched perpendicular to the background magnetic field ($\boldsymbol{B}_0$) and weakly modulated by CD. In contrast, fast modes are subjected to a more significant CD modulation. Fast modes exhibit a weak, scale-independent anisotropy above the CD truncation scale. Below the CD truncation scale, the anisotropy of fast modes enhances as wavenumbers increase. As a result, fast-mode fractions in the total energy of compressible modes decrease with the increase of perpendicular wavenumber (to $\boldsymbol{B}_0$) or wave propagation angle. Our findings reveal how the turbulence cascade is shaped by CD and its consequences for anisotropies in the space environment.

Unified Astronomy Thesaurus concepts: Interplanetary turbulence (830); Interplanetary physics (827); Space plasmas (1544); Plasma astrophysics (1261); Magnetohydrodynamics (1964)

1. Introduction

Plasma turbulence, particularly its compressible component, plays a crucial role in numerous astrophysical processes, such as the heating and acceleration of the solar wind, cosmic-ray transport, and star formation (Bruno & Carbone 2013; Yan 2022). The current model of plasma turbulence is typically characterized by three steps: (1) energy injection on large scales (Matthaeus et al. 1986; Cho & Lazarian 2003), (2) an inertial energy cascade following some self-similar power-law scaling (Ng & Bhattacharjee 1996; Horbury et al. 2008), and (3) dissipation caused by certain kinetic physical processes on small scales (Leamon et al. 1998, 1999; Yan & Lazarian 2002; Alexandrova et al. 2009; Sahraoui et al. 2009). The inertial energy cascade, the most characteristic signature of magneto-hydrodynamic (MHD) turbulence, has been effectively described using incompressible MHD models such as the isotropic theory (Iroshnikov 1963; Kraichnan 1965) and the scale-dependent anisotropic turbulence theory (Goldreich & Sridhar 1995). The nearly incompressible theory has also been used to explain some phenomena related to compressible solar wind turbulence (Zank & Matthaeus 1992, 1993). However, within the inertial energy cascade, compressible MHD turbulence undergoes damping processes (Barnes 1966, 1967; Yan & Lazarian 2004; Suzuki et al. 2006), which are still not completely understood. Fully comprehending how damping affects compressible MHD turbulence is integral for portraying turbulence in actual plasma environments.

One prominent feature of MHD turbulence is the anisotropy, which has been extensively studied through simulations and satellite observations (Cho & Vishniac 2000; Stawarz et al. 2009; Oughton et al. 2015; Huang et al. 2017; Andrés et al. 2022; Jiang et al. 2023). In a homogeneous plasma with a uniform background magnetic field ($\boldsymbol{B}_0$), small-amplitude compressible MHD fluctuations can be decomposed into three linear eigenmodes (namely, Alfvén mode, slow magnetosonic mode, and fast magnetosonic mode; Glassmeier et al. 1995; Cho & Lazarian 2003; Chaston et al. 2020; Makwana & Yan 2020; Zhu et al. 2020; Zhao et al. 2021, 2022, 2023). The linear independence among the three MHD eigenmodes enables individual analysis of their statistical properties of small-amplitude plasma turbulence (Cho & Lazarian 2003, 2005). The composition of MHD modes significantly affects the energy cascade and observational turbulence statistics (Andrés et al. 2018; Makwana & Yan 2020; Zhang et al. 2020; Brodiano et al. 2021; Zhao et al. 2022; Malik et al. 2023; Yuen et al. 2023, 2023). Based on the modern theory of compressible MHD turbulence, the Alfvén and slow modes are expected to follow a

[6] Corresponding author.

cascade with scale-dependent anisotropy $k_\parallel \propto k_\perp^{2/3}$, where $k_\perp$ and $k_\parallel$ are wavenumbers perpendicular and parallel to $\boldsymbol{B}_0$ (Goldreich & Sridhar 1995; Lithwick & Goldreich 2001). In contrast, fast modes are expected to show isotropic behaviors and cascade like the acoustic wave (Cho & Lazarian 2003; Galtier 2023). These theoretical conjectures have been confirmed by numerical simulations (Cho & Lazarian 2005; Makwana & Yan 2020).

Earlier theoretical studies have demonstrated a strong propagation angle dependence on collisionless damping (CD) and viscous damping influencing the three-dimensional (3D) energy distributions (Yan & Lazarian 2004, 2008; Yan et al. 2004; Petrosian et al. 2006). The CD leads to the rapid dissipation of plasma waves by wave–particle interactions via gyroresonance, transit time damping, or Landau resonance (Yan & Lazarian 2004, 2008). Despite theoretical predictions, direct observations demonstrating how CD modulates the statistics of compressible MHD modes are still lacking, primarily due to the limited satellite measurements. Thanks to the availability of spatial information from four Cluster spacecraft, we can estimate the energy distributions of compressible turbulence. Although early Cluster data are relatively old, we use a novel, improved MHD-mode decomposition method to analyze them. This study compares the theoretical CD rate and observed energy distributions, providing the first observational evidence of substantial CD modulation on small-amplitude compressible MHD turbulence.

2. Overview

Figure 1 shows an overview of Cluster observations in Earth's magnetosheath during 19:00–14:00 UT on 2003 December 2–3 in geocentric solar ecliptic (GSE) coordinates. During this time interval, the Cluster mission is in a tetrahedral configuration with a relative separation $d_{sc} \sim 200$ km (around three proton inertial length $d_i \sim 74$ km), enabling us to perform a multipoint analysis of MHD turbulence. To ensure low-frequency (large-scale) measurements while the mean magnetic field $\boldsymbol{B}_0$ approaches the local background magnetic field, we split the whole time interval into several time windows with a 5 hr length and a 5 minute moving step. Performing an MHD-mode decomposition during 23:00–10:00 UT (the red bar on the top of Figure 1) is applicable for the following reasons. First, the background magnetic field measured by the Fluxgate Magnetometer (FGM; Balogh et al. 1997) and proton plasma parameters measured by the Cluster Ion Spectrometry's Hot Ion Analyzer (CIS-HIA; Rème et al. 2001) are relatively stable, as shown in Figures 1(a)–(d). Fluctuations are approximately stationary and homogeneous based on the analysis of correlation functions (see Appendix A). Additionally, the fluctuations are in a well-developed state, as shown in Figure 1(f), where the spectral slopes (α_{V_p} and α_B) of the trace proton velocity and magnetic field power at spacecraft frequency $f_{sc} \sim [0.001\,\text{Hz},\ 0.1 f_{ci}]$ range between $-5/3$ and $-3/2$ (the proton gyrofrequency $f_{ci} \sim 0.24$ Hz). The trace proton velocity and magnetic field power are calculated through the fast Fourier transform with five-point smoothing in each time window. Figure 1(g) shows that the turbulent Alfvén Mach number ($M_{A,turb} = \delta V_p / V_A$) and relative amplitudes of magnetic field fluctuations ($\delta B/B_0$) are smaller than unity, indicating that the nonlinear terms ($\delta \boldsymbol{V}_p^2$, $\delta \boldsymbol{B}^2$) are smaller than the linear terms ($V_A \delta \boldsymbol{V}_p$, $B_0 \delta \boldsymbol{B}$). Thus, the assumption of small-amplitude approximation is satisfied. Table 1 lists the values of the background physical parameters for our analysis.

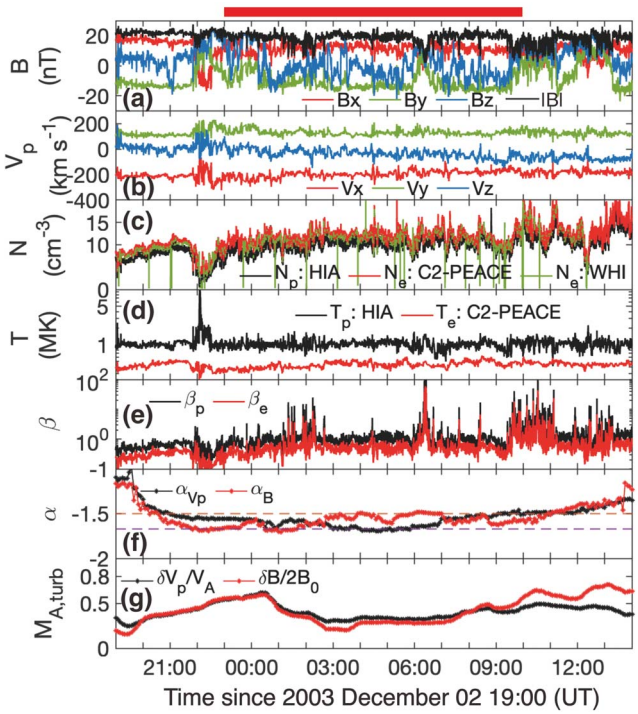

Figure 1. An overview of fluctuations measured by Cluster-1. The red bar on the top marks the interval during 23:00–10:00 UT on 2003 December 2–3. (a) Magnetic field. (b) Proton bulk velocity. (c) Cross-check of proton density from CIS-HIA (black) and electron density from the Plasma Electron And Current Experiment (Johnstone et al. 1997) on board Cluster-2 (red) and from Waves of High frequency and Sounder for Probing of Electron density by Relaxation (Décréau et al. 1997; green). (d) and (e) Temperature and plasma β (the ratio between thermal and magnetic pressures). (f) Spectral slopes (α) of trace proton velocity and magnetic field power. The horizontal dashed lines represent $\alpha = -5/3$ and $-3/2$. (g) $\delta V_p/V_A$ (black) and $\delta B/(2B_0)$ (red), where δV_p and δB are the rms proton velocity and magnetic field fluctuations, respectively.

3. MHD-mode Decomposition

Previous studies suggest that strong turbulence develops scale-dependent anisotropy in the local frame of reference (Cho & Vishniac 2000). In order to trace the local frame anisotropy, we split the whole time interval into several time windows. In each time window, we separate compressible fluctuations into slow and fast modes (Alfvén modes are analyzed in Zhao et al. 2023) and establish 3D wavenumber distributions. We decompose the MHD eigenmodes by combining three methods: the linear decomposition method (Cho & Lazarian 2003; Zhao et al. 2021), the singular value decomposition (SVD) method (Santolík et al. 2003), and multispacecraft timing analysis (Grinsted et al. 2004). The combination of the three methods allows direct retrieval of energy wavenumber distributions from the observed frequency distributions independent of any spatiotemporal hypothesis (e.g., the Taylor hypothesis; Taylor 1938).

First, we obtain wavelet coefficients of proton velocity, magnetic field, and proton density using Morlet-wavelet transforms (Grinsted et al. 2004). To eliminate the edge effect resulting from finite-length time series, we perform wavelet transforms twice the length of the studied period and remove the affected periods.

Second, wavevector directions ($\hat{\boldsymbol{k}}_{SVD}(t, f_{sc})$) are calculated by creating a matrix equation ($\boldsymbol{A} \cdot \hat{\boldsymbol{k}}_{SVD} = 0$) equivalent to the

Table 1
Physical Parameters for This Observed Event

Start Time (UT)	End Time (UT)	B_0 (nT)	N_0 (cm^{-3})	V_A (km s^{-1})	V_S (km s^{-1})	β_p	V_{Te} (km s^{-1})	d_i (km)	f_{ci} (Hz)
2003-12-2/23:00	2003-12-3/10:00	19.2	10.1	133	121	1.0	2567	74	0.24

Note. Outliers, defined as elements more than three scaled median absolute deviations (1.48 · median($|X - \text{median}(X)|$)) from the median, are replaced with the linear interpolation of neighboring nonoutlier values.

linearized Gauss law ($\boldsymbol{B} \cdot \hat{\boldsymbol{k}}_{\rm SVD} = 0$). The matrix $\boldsymbol{A}$ (6×3) consists of the real and imaginary parts of the spectral matrix S_{mn}, where $S_{mn} = B_m B_n^*$; $m = X, Y, Z$; and $n = X, Y, Z$ are three components in GSE coordinates (for details, see Equation (8) in Santolík et al. 2003). The energy density at each time t and $f_{\rm sc}$ is a mixture of fluctuations with different dispersion relations (and thus different wavevectors). However, the SVD method only gives the best-estimated direction of the wavevector sum, not the wavevector magnitude. The unit wavevectors calculated by SVD and mean magnetic field are averaged over four Cluster spacecraft: $\boldsymbol{k}_{\rm SVD} = \frac{1}{4}\sum_{i=1,2,3,4}\hat{\boldsymbol{k}}_{{\rm SVD},Ci}$ and $\boldsymbol{B}_0 = \frac{1}{4}\sum_{i=1,2,3,4}\boldsymbol{B}_{0,Ci}$, where Ci denotes the four Cluster spacecraft.

Third, the $\hat{k}\hat{b}_0$ coordinates are determined by $\hat{\boldsymbol{k}}_{\rm SVD} = \boldsymbol{k}_{\rm SVD}/|\boldsymbol{k}_{\rm SVD}|$ and $\hat{\boldsymbol{b}}_0 = \boldsymbol{B}_0/|\boldsymbol{B}_0|$ (see Figure 7(a) in Appendix B). The axis basis vectors are $\hat{\boldsymbol{e}}_{\parallel} = \hat{\boldsymbol{b}}_0$, $\hat{\boldsymbol{e}}_{\perp 1} = \hat{\boldsymbol{k}}_{\rm SVD} \times \hat{\boldsymbol{b}}_0/|\hat{\boldsymbol{k}}_{\rm SVD} \times \hat{\boldsymbol{b}}_0|$, and $\hat{\boldsymbol{e}}_{\perp 2} = \hat{\boldsymbol{b}}_0 \times (\hat{\boldsymbol{k}}_{\rm SVD} \times \hat{\boldsymbol{b}}_0)/|\hat{\boldsymbol{b}}_0 \times (\hat{\boldsymbol{k}}_{\rm SVD} \times \hat{\boldsymbol{b}}_0)|$. The complex vectors (wavelet coefficients of the proton velocity and magnetic field) are transformed from GSE coordinates to $\hat{k}\hat{b}_0$ coordinates.

Fourth, magnetic field data are measured by four Cluster spacecraft, whereas proton plasma data are only available on Cluster-1 during the analyzed period. Thus, magnetic field power is calculated by $P_{B_l}(t, f_{\rm sc}) = \frac{1}{4}\sum_{i\ =\ 1,2,3,4} W_{B_l,Ci} W^*_{B_l,Ci}$, where l represents $\hat{\boldsymbol{e}}_{\parallel}$, $\hat{\boldsymbol{e}}_{\perp 1}$, and $\hat{\boldsymbol{e}}_{\perp 2}$. The proton velocity and proton density power are calculated by $P_{V_l}(t, f_{\rm sc}) = W_{V_l,C1} W^*_{V_l,C1}$ and $P_N(t, f_{\rm sc}) = W_{N,C1} W^*_{N,C1}$. W_{V_l}, W_{B_l}, and W_N represent wavelet coefficients of proton velocity, magnetic field, and proton density fluctuations.

Fifth, noticing that SVD does not give the magnitude of the wavevectors, we utilize multispacecraft timing analysis based on phase differences between magnetic wavelet coefficients to determine the wavevectors ($\boldsymbol{k}_{B_l}(t, f_{\rm sc})$; Pincon & Glassmeier 1998). The magnetic field data are interpolated to a uniform time resolution of 2^3samples s^{-1} for sufficient time resolutions. We consider that the wave front is moving in the direction $\hat{\boldsymbol{n}}$ with velocity V_w. The wavevectors $\boldsymbol{k}_{B_l} = 2\pi f_{\rm sc}\boldsymbol{m}$ are determined by phase differences of the magnetic field B_l component,

$$\begin{pmatrix} \boldsymbol{r}_2 - \boldsymbol{r}_1 \\ \boldsymbol{r}_3 - \boldsymbol{r}_1 \\ \boldsymbol{r}_4 - \boldsymbol{r}_1 \end{pmatrix} \boldsymbol{m} = \begin{pmatrix} \delta t_2 \\ \delta t_3 \\ \delta t_4 \end{pmatrix}, \tag{1}$$

where the vector $\boldsymbol{m} = \hat{\boldsymbol{n}}/V_w$, and Cluster-1 has arbitrarily been taken as the reference (Pincon & Glassmeier 1998). The left side of Equation (1) represents the relative spacecraft separations. The right side of Equation (1) represents the weighted average time delays, estimated by the ratio of six phase differences ($\phi_{ij} = \arctan(\mathcal{S}(W^{ij}_{B_l}), \mathcal{R}(W^{ij}_{B_l}))$) to the angular frequencies ($\omega_{\rm sc} = 2\pi f_{\rm sc}$), where ϕ_{ij} is from all spacecraft pairs ($ij = 12, 13, 14, 23, 24, 34$)). $\mathcal{S}$ and $\mathcal{R}$ are the imaginary and real parts of the cross-correlation coefficients, respectively. Four Cluster spacecraft provide six cross-correlation coefficients for each B_l component (Grinsted et al. 2004), i.e., $W^{12}_{B_l} = \langle W_{B_l,C1} W^*_{B_l,C2}\rangle$, $W^{13}_{B_l} = \langle W_{B_l,C1} W^*_{B_l,C3}\rangle$, $W^{14}_{B_l} = \langle W_{B_l,C1} W^*_{B_l,C4}\rangle$, $W^{23}_{B_l} = \langle W_{B_l,C2} W^*_{B_l,C3}\rangle$, $W^{24}_{B_l} = \langle W_{B_l,C2} W^*_{B_l,C4}\rangle$, and $W^{34}_{B_l} = \langle W_{B_l,C3} W^*_{B_l,C4}\rangle$, where $\langle ... \rangle$ denotes a time average over 256 s for the reliability of the phase differences.

It is worth noting that multispacecraft timing analysis determines the actual wavevectors of each B_l component ($\boldsymbol{k}_{B_l} = \boldsymbol{k}_{B_\parallel}$, $\boldsymbol{k}_{B_{\perp 1}}$, and $\boldsymbol{k}_{B_{\perp 2}}$), different from the best-estimated direction of the sum of the wavevectors determined by three magnetic field components ($\hat{\boldsymbol{k}}_{\rm SVD}$). Therefore, $\boldsymbol{k}_{B_l}$ is not completely aligned with $\hat{\boldsymbol{k}}_{\rm SVD}$. During the analyzed period, Alfvén-mode fluctuations dominate ($\delta V_{\perp 1}/\delta V_p \sim 60\%$); thus, the $\hat{k}\hat{b}_0$ coordinates determined by $\hat{\boldsymbol{k}}_{\rm SVD}$ are little affected only when $\boldsymbol{k}_{B_\parallel}$ and $\boldsymbol{k}_{B_{\perp 2}}$ are coplanar with the $\hat{k}\hat{b}_0$ plane. In other words, $\boldsymbol{k}_{B_\parallel}$ and $\boldsymbol{k}_{B_{\perp 2}}$ should deviate from the $\hat{k}\hat{b}_0$ plane by a small angle. To simplify, we shall write $\boldsymbol{k}$ as a shorthand notation for $\boldsymbol{k}_{B_l}$ and define the angle between $\boldsymbol{k}$ and the $\hat{k}\hat{b}_0$ plane as η. This study only analyzes fluctuations with small η. With a more stringent η constraint, the mode decomposition between the slow and fast modes becomes more complete, whereas the uncertainties caused by limited samplings increase. We discuss the uncertainties resulting from the η deviation in Section 6 and Appendix C and present spectral results under $\eta < 20°$ in the main text. Overall, the main properties of energy spectra of slow and fast modes do not significantly change as η varies.

Sixth, we construct a set of $200 \times 200 \times 200$ bins to obtain 3D wavenumber distributions of energy density ($D_{\epsilon_l}(\boldsymbol{k})$), where $\epsilon = V$, B, N represents proton velocity (V), magnetic field (B), and proton density (N) fluctuations. In each bin, the fluctuations have approximately the same wavenumber. To cover all MHD wavenumbers and ensure measurement reliability, we restrict our analysis to fluctuations with $1/(100d_{\rm sc}) < k < 1.1 \times 0.1/d_i$ and $2/t^* < f_{\rm rest} < f_{\rm ci}/2$, where the wavenumber $k = \sqrt{k_\parallel^2 + k_\perp^2}$, t^* is the time window length, $f_{\rm rest} = f_{\rm sc} - \boldsymbol{k} \cdot \boldsymbol{V}/(2\pi)$ is the frequency in the plasma flow frame, and $\boldsymbol{V}$ is approaching the proton bulk velocity due to negligible spacecraft velocity. Fluctuations beyond the wavenumber and frequency ranges are set to zero. $D_{\epsilon_l}(\boldsymbol{k})$ is calculated by averaging $P_{\epsilon_l}(t, f_{\rm sc})$ over effective time points in all time windows and integrating over $f_{\rm sc}$.

Seventh, the energy density of the fast and slow modes is calculated by $D_{\epsilon,\pm} = \delta\epsilon^2_{k,\pm}$, where "+" is for fast modes and "−" is for slow modes. The velocity fluctuations of the fast and slow modes in wavevector space are calculated by

$$\delta V_{k,\pm} = \langle |\delta V_{k,\parallel}\hat{\boldsymbol{e}}_\parallel \cdot \hat{\boldsymbol{\xi}}_\pm \pm \delta V_{k,\perp 2}\hat{\boldsymbol{e}}_{\perp 2} \cdot \hat{\boldsymbol{\xi}}_\pm| \rangle, \tag{2}$$

where $\langle ... \rangle$ denotes the average over effective time points in all time windows. In wavevector space, $\delta V_{k,\parallel} = \sqrt{\sum_{f_{\rm sc}} D_{V_\parallel}(\boldsymbol{k}, f_{\rm sc}, t)}\exp(2\pi i\phi_1(\boldsymbol{k}, f_{\rm sc}, t))$, and $\delta V_{k,\perp 2} = \sqrt{\sum_{f_{\rm sc}} D_{V_{\perp 2}}(\boldsymbol{k}, f_{\rm sc}, t)}\exp(2\pi i\phi_2(\boldsymbol{k}, f_{\rm sc}, t))$, where ϕ_1 and ϕ_2 are phase angles. The phase angle of turbulence fluctuations in a homogeneous system is usually assumed to be a uniform

distribution. Therefore, we take ϕ_1 and ϕ_2 to be uniform in $[0, 2\pi]$, and Equation (2) can be simplified to

$$\delta V_{k,\pm} \propto |\sqrt{D_{V_\parallel}(\boldsymbol{k})}\cos\zeta_{\hat{e}_\parallel\hat{\xi}_\pm} \pm \sqrt{D_{V_{\perp 2}}(\boldsymbol{k})}\sin\zeta_{\hat{e}_\parallel\hat{\xi}_\pm}|,$$

where $\zeta_{\hat{e}_\parallel\hat{\xi}_\pm}$ is the angle between $\hat{\boldsymbol{e}}_\parallel$ and $\hat{\boldsymbol{\xi}}_\pm$. Fast- and slow-mode displacement vectors are given by Cho & Lazarian (2003),

$$\boldsymbol{\xi}_\pm \propto (-1+\alpha \pm \sqrt{A})k_\parallel\hat{\boldsymbol{e}}_\parallel + (1+\alpha\pm\sqrt{A})k_\perp\hat{\boldsymbol{e}}_{\perp 2}. \quad (3)$$

The unit displacement vectors $\hat{\boldsymbol{\xi}}_\pm = \boldsymbol{\xi}_\pm/|\boldsymbol{\xi}_\pm|$. The parameter $A = (1+\alpha)^2 - 4\alpha\cos\theta$, where $\alpha = V_S^2/V_A^2$, V_A is the Alfvén speed, V_S is the sound speed, and θ is the angle between $\boldsymbol{k}$ and $\boldsymbol{B}_0$.

Fast- and slow-mode magnetic field and proton density fluctuations are estimated as (Cho & Lazarian 2003)

$$\delta B_{k,\pm} = B_0\frac{\delta V_{k,\pm}}{V_{ph,\pm}}|\hat{\boldsymbol{e}}_\parallel \times \hat{\boldsymbol{\xi}}_\pm|, \quad (4)$$

$$\delta N_{k,\pm} = N_0\frac{\delta V_{k,\pm}}{V_{ph,\pm}}\hat{\boldsymbol{k}}\cdot\hat{\boldsymbol{\xi}}_\pm. \quad (5)$$

The unit wavevector $\hat{\boldsymbol{k}} = \boldsymbol{k}/|\boldsymbol{k}|$, and N_0 is the background proton density. Fast- and slow-mode phase speeds are given by Hollweg (1975),

$$V_{\mathrm{ph},\pm}^2 = \frac{1}{2}(V_S^2+V_A^2) \pm [(V_S^2+V_A^2)^2 - 4V_S^2V_A^2\cos^2\theta]^{1/2}. \quad (6)$$

Appendix D shows that the decomposed magnetic field and density fluctuations (inferred from proton velocity fluctuations via Equations (4) and (5); Cho & Lazarian 2003) match those directly measured by the FGM and CIS-HIA instruments, indicating the reliability of MHD-mode decomposition. All symbols used in this study are summarized in Table 2 (see Appendix B).

4. Slow Modes

In Figure 2(a), we observe that the normalized wavenumber distributions of the proton velocity energy of slow modes ($\hat{D}_{V-}$; colored contours) are prominently distributed along the $k_\perp$ axis, suggesting a faster cascade in the perpendicular direction. We also observe an increase in the anisotropy of energy distributions with the increasing wavenumbers. These observations indicate that smaller eddies of slow modes are more elongated along $\boldsymbol{B}_0$, in agreement with theoretical expectations and simulation results (Cho & Vishniac 2000; Makwana & Yan 2020). The anisotropic behaviors of slow modes found here are roughly similar to those for Alfvén modes (Zhao et al. 2023), presumably because slow modes passively mimic Alfvén modes (Cho & Lazarian 2003, 2005).

The slow-mode theoretical damping rate (γ_{slow}) can be expressed as a function of wavenumber,

$$\gamma_{\mathrm{slow}} = \frac{|\boldsymbol{k}|V_S}{2|\cos\theta|}\left(\frac{1}{8}\pi\frac{m_e}{m_p}\right)^{1/2}\left(1 - \frac{\cos 2\theta[(V_S^2/V_A^2)\cos 2\theta - 1]}{[1+V_S^4/V_A^4 - 2(V_S^2/V_A^2)\cos 2\theta]^{1/2}}\right), \quad (7)$$

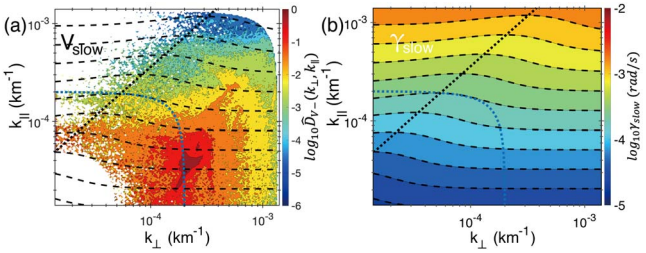

Figure 2. Slow modes. (a) Wavenumber distributions of slow-mode proton velocity energy ($\hat{D}_{V-}$; colored contours) and damping rate (γ_{slow}; black dashed curves). $\hat{D}_{V-} = D_{V-}/D_{V-,\max}$ is normalized by the maximum energy density, where $\hat{D}_{V-}$ less than 6 orders of maximum magnitude or at $k < 1/(100d_{\mathrm{sc}}) = 5\times10^{-5}$ km^{-1} is set to zero. (b) Wavenumber distributions of γ_{slow}. The black dotted line marks the peak line of γ_{slow} contours. The blue dotted curve in each panel marks an isotropic contour at $k = 2\times10^{-4}$ km^{-1} as a reference.

where the background parameters are listed in Table 1, and m_e and m_p are the electron and proton mass, respectively (Oraevsky 1983). As shown in Figure 2(b) or Equation (7), γ_{slow} is very sensitive to the changes of $k_\parallel$ but not $k_\perp$. Interestingly enough, the constant contours of γ_{slow} achieve peak values along the black dotted line in Figure 2(b). As it turns out, this special feature predicted by Equation (7) is a notable signature of the CD modulation on energy spectra.

In Figure 2(a), γ_{slow} contours (black dashed curves) are superposed on the $\hat{D}_{V-}$ spectrum (colored contours). The similar pattern of energy isocontours peaking along the black dotted line is also recognized in the upper left corner of the $\hat{D}_{V-}$ spectrum. This special consistency between the $\hat{D}_{V-}$ spectrum and γ_{slow} contours is not seen in the Alfvén-mode counterpart (Zhao et al. 2023), where Alfvén-mode energy steadily decreases with $k_\perp$ at each $k_\parallel$. Combined with the previous work (Zhao et al. 2023), our analysis in Figure 2 suggests that CD can weakly modulate the energy distributions of slow modes but has little influence on those of Alfvén modes. Nevertheless, we note that this weak CD modification can only be observed in the upper left corner of the $\hat{D}_{V-}$ spectrum, which is likely because (1) γ_{slow} increases with the increase of $k_\parallel$, and (2) γ_{slow} plays a limited role in shaping slow-mode energy spectra, since the slow-mode cascading rate $\tau_{\mathrm{slow}}^{-1}$) is much larger than γ_{slow} ($\tau_{\mathrm{slow}}^{-1}/\gamma_{\mathrm{slow}} \geqslant 10$), where $\tau_{\mathrm{slow}}^{-1} = k_\perp^{2/3}L_0^{-1/3}V_A$ (Lithwick & Goldreich 2001; Cho & Lazarian 2003). To simplify, the injection scale $L_0 = T_c\delta V_0$, the correlation time T_c determined by correlation functions is around 2300 s (Zhao et al. 2023), and the injection fluctuating velocity δV_0 is approximated as $M_{\mathrm{A,turb}}V_A \sim 40$ km s^{-1}.

To further estimate the anisotropy of the fast and slow modes, we define a parameter

$$R_\pm(k') = \frac{D_{V\pm}(k_\perp = k')}{D_{V\pm}(k_\parallel = k')} \quad (8)$$

for a given wavenumber k', where the reduced perpendicular and parallel wavenumber distributions of the energy density are calculated by

$$D_\epsilon \pm (k_\perp) \sim \sum_{k_\parallel=k_{\mathrm{low}}}^{k_\parallel=k_{\mathrm{upp}}} D_\epsilon \pm (k_\perp, k_\parallel), \quad (9)$$

$$D_\epsilon \pm (k_\parallel) \sim \sum_{k_\perp=k_{\mathrm{low}}}^{k_\perp=k_{\mathrm{upp}}} D_\epsilon \pm (k_\perp, k_\parallel). \quad (10)$$

The integral upper limit $k_{\rm upp} = 0.1/d_i \sim 1.4 \times 10^{-3}\,{\rm km}^{-1}$, and the integral lower limit $k_{\rm low} = 1/(100 d_{\rm sc}) \sim 5 \times 10^{-5}\,{\rm km}^{-1}$.

Figure 3(a) shows a strong correlation between $\log_{10} R_-(k')$ and $\log_{10} \gamma_{{\rm slow},\parallel}(k')$ with a correlation coefficient of 0.97, where the parallel damping rate $\gamma_{{\rm slow},\parallel}(k')$ is calculated by averaging $\gamma_{\rm slow}(k_\perp, k_\parallel = k')$ over $k_\perp$ for a given wavenumber k'. Moreover, the positive index of the power-law fit (0.46 ± 0.28) indicates that more significant anisotropy of slow modes corresponds to larger values of $\gamma_{\rm slow}$ along $\boldsymbol{B}_0$.

5. Fast Modes

In Figure 4(a), we observe that the normalized wavenumber distributions of the proton velocity of fast modes ($\hat{D}_{V+}$; colored contours) show more isotropic features than slow modes. Figure 4(b) shows that wavenumber distributions of the fast-mode cascading rate ($\tau_{\rm fast}^{-1}$) present a scale-independent anisotropy, where $\tau_{\rm fast}^{-1} \sim (k/L_0)^{1/2} \delta V_0^2 / V_{{\rm ph},+}$ (Yan & Lazarian 2004). When $\omega_{\rm fast}/k_\parallel \ll V_{Te}$, the fast-mode theoretical damping rate is given by Oraevsky (1983):

$$\gamma_{\rm fast} = \frac{|\boldsymbol{k}| V_S}{2|\cos\theta|}\left(\frac{1}{8}\pi\frac{m_e}{m_p}\right)^{1/2} \left(1 + \frac{\cos 2\theta\,[(V_S^2/V_A^2)\cos 2\theta - 1]}{[1 + V_S^4/V_A^4 - 2(V_S^2/V_A^2)\cos 2\theta]^{1/2}}\right). \quad (11)$$

When $\omega_{\rm fast}/k_\parallel \gg V_{Te}$,

$$\gamma_{\rm fast} = \left(\frac{1}{8}\pi\right)^{1/2} \omega_{\rm fast} \frac{m_e V_{Te} \sin^2\theta}{m_p V_A |\cos\theta|} \exp\left(-\frac{\omega_{\rm fast}^2}{2k_\parallel^2 V_{Te}^2}\right), \quad (12)$$

where $\omega_{\rm fast}$ is the fast-mode frequency, $V_{Te} = \sqrt{k_{\rm B} Te/m_e}$ is the electron thermal speed, and $k_{\rm B}$ is the Boltzmann constant. Figure 4(c) shows $\gamma_{\rm fast}$ calculated by combining Equation (11) at $\omega_{\rm fast}/k_\parallel \leqslant V_{Te}$ and Equation (12) at $\omega_{\rm fast}/k_\parallel \geqslant V_{Te}$, where the background parameters are listed in Table 1. With increasing $k_\perp$, $\gamma_{\rm fast}$ sharply enhances and is up to $0.9\,{\rm rad\,s}^{-1}$ in the bottom right corner where θ approaches 90°, indicating that fast modes undergo more severe CD damping and rapid dissipation at larger $k_\perp$ and θ.

We superpose the contours of $\tau_{\rm fast}^{-1}$ (black solid curves) and $\gamma_{\rm fast}$ (purple dashed curves) on the $\hat{D}_{V+}$ spectrum in Figure 4(a). Different from slow modes, fast modes exhibit CD truncation scales (kc; the red line) that are obtained by equating $\tau_{\rm fast}^{-1}$ and $\gamma_{\rm fast}$ (Yan & Lazarian 2008). On kc scales, turbulence cascade and CD play a comparable role in shaping energy distributions. (1) At $k < 2 \times 10^{-4}\,{\rm km}^{-1}$ (blue dotted curve), the $\hat{D}_{V+}$ spectrum agrees well with the $\tau_{\rm fast}^{-1}$ contours on the left side of the red line (above kc; $\tau_{\rm fast}^{-1} > \gamma_{\rm fast}$). The weak, scale-independent anisotropy of the $\hat{D}_{V+}$ spectrum suggests that fast-mode energy distributions do not depend heavily on $\boldsymbol{B}_0$, consistent with numerical simulations and theoretical analysis of fast modes (Cho & Lazarian 2003; Galtier 2023). (2) At $k > 2 \times 10^{-4}\,{\rm km}^{-1}$, with increasing $k_\perp$, the magnitude of the $\hat{D}_{V+}$ spectrum generally decreases, whereas $\gamma_{\rm fast}$ sharply increases on the right side of the red line (below kc; $\tau_{\rm fast}^{-1} < \gamma_{\rm fast}$). These results imply that $\gamma_{\rm fast}$ likely plays a more crucial role in shaping the fast-mode energy spectrum on smaller scales. Above all, these findings support the theoretical prediction that energy distributions of fast-mode turbulence are shaped by the forcing on large scales and the damping on small scales.

Figure 3(b) shows that the correlation coefficient between $\log_{10} R_+(k')$ and $\log_{10} \gamma_{{\rm fast},\perp}(k')$ is 0.97, and their power-law fit

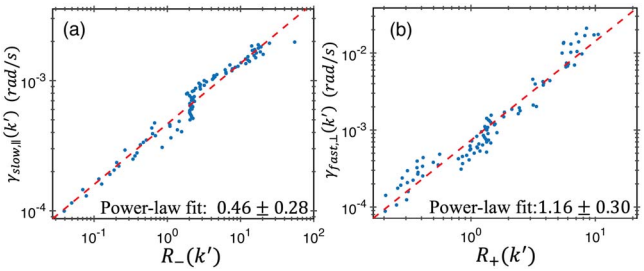

Figure 3. The relations between the anisotropy of energy distributions ($R_\pm$ estimated by Equation (8)) and CD rates ($\gamma_{\rm slow}$ and $\gamma_{\rm fast}$ estimated by Equations (7), (11), and (12)). (a) R_- vs. $\gamma_{{\rm slow},\parallel}$. (b) R_+ vs. $\gamma_{{\rm fast},\perp}$. The red dashed lines represent power-law fits. The shown average values and standard deviations of power-law indices are obtained using a least-squares fit to the relations on a log-log plot.

is 1.16 ± 0.30, where the perpendicular damping rate $\gamma_{{\rm fast},\perp}(k')$ is obtained by averaging $\gamma_{\rm fast}(k_\perp = k', k_\parallel)$ over $k_\parallel$ for a given wavenumber k'. This strong correlation between CD and anisotropy of fast modes further indicates that CD plays an increasingly important role in shaping the energy distributions of fast modes as $k_\perp$ increases.

6. Fast-mode Fraction Relative to the Total Energy of Compressible Modes

Figure 5 shows the ratio of fast-mode energy to the total energy of compressible modes as a function of $k_\perp$ and θ, which is defined as $F_{{\rm fast},\epsilon} = \frac{D_{\epsilon+}}{D_{\epsilon+} + D_{\epsilon-}}$, where $\epsilon = V, B, N$ represents proton velocity (V), magnetic field (B), and proton density (N) fluctuations. For easier reference, we name this ratio the "fast-mode fraction." The shaded regions in both panels of Figure 5 represent standard deviations of the results for data sets from $\eta < 10°$ to 30°, binning $\Delta\eta = 1°$. It is evident from Figure 5 that the η deviation does not affect the general trend of $F_{{\rm fast},\epsilon}$ as functions of $k_\perp$ and θ. In Figure 5(a), $F_{{\rm fast},\epsilon}$ has a decreasing trend as $k_\perp$ increases up to $k_\perp < 3 \times 10^{-4}\,{\rm km}^{-1}$, after which $F_{{\rm fast},\epsilon}$ is roughly a constant with a small value [0.1, 0.2]. Furthermore, regression analysis suggests that the three fractions $F_{{\rm fast},\epsilon}$ have similar power-law scaling at $k_\perp < 3 \times 10^{-4}\,{\rm km}^{-1}$, indicating that CD damps out the fast-mode fraction consistently over all MHD observables.

We perform a similar analysis on $F_{{\rm fast},\epsilon}$ to θ to explore whether there is an angle dependence for CD modulation. Figure 5(b) demonstrates that, at small θ, fast modes dominate magnetic field fluctuations, whereas slow modes dominate proton density fluctuations. As θ increases, the fast-mode fractions of the three parameters gradually become comparable. Moreover, the linear decrease of $F_{{\rm fast},V}$ as θ increases is consistent with higher $\gamma_{\rm fast}$ at larger θ. The different θ dependencies in $F_{{\rm fast},B}$ and $F_{{\rm fast},N}$ can be attributed to the angle dependence in the calculations of Equations ((4) and (5)), wherein magnetic field and proton density fluctuations are inferred from proton velocity fluctuations.

7. Summary

This study presents the first observational evidence of substantial CD modulation on a compressible MHD turbulence cascade. Utilizing an improved MHD-mode decomposition technique, we are able to obtain wavenumber distributions of slow and fast modes via four Cluster spacecraft measurements in Earth's magnetosheath. Our findings are summarized below.

(1) Wavenumber distributions of slow modes are mainly stretched perpendicular to $\boldsymbol{B}_0$ and weakly modulated by CD. In contrast, fast modes are subject to a more significant CD modulation. Fast modes exhibit a weak, scale-independent

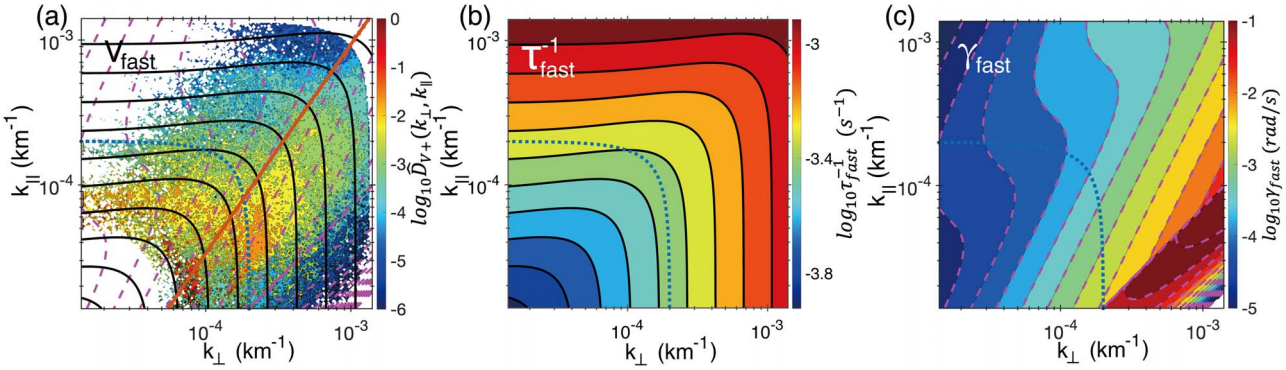

Figure 4. Fast modes. (a) Wavenumber distributions of fast-mode proton velocity energy ($\hat{D}_{V+}$; colored contours), cascading rate ($\tau^{-1}_{\rm fast}$; black solid curves), and damping rate ($\gamma_{\rm fast}$; purple dashed curves). To facilitate the comparison, the velocity energy spectrum is normalized by the same constant as the slow modes in Figure 2(a). $\hat{D}_{V+}$ less than 6 orders of magnitude or at $k < 1/(100d_{\rm sc}) = 5 \times 10^{-5}$ km^{-1} is set to zero. The red line marks the fast-mode CD truncation scales. (b) Wavenumber distributions of $\tau^{-1}_{\rm fast}$. (c) Wavenumber distributions of $\gamma_{\rm fast}$. The blue dotted curve in each panel marks an isotropic contour at $k = 2 \times 10^{-4}$ km^{-1} as a reference.

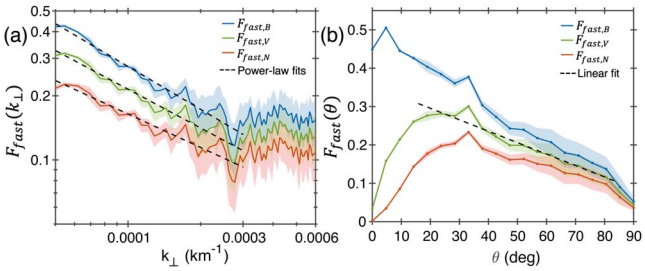

Figure 5. The fast-mode fraction $F_{{\rm fast},\epsilon} = \frac{D_{\epsilon+}}{D_{\epsilon+}+D_{\epsilon-}}$ calculated with $k_{\rm low} < k_{\perp}$, $k_{\parallel} < k_{\rm upp}$(see Equations (9) and (10)). (a) $F_{{\rm fast},\epsilon}(k_{\perp})$ vs. $k_{\perp}$. (b) $F_{{\rm fast},\epsilon}(\theta)$ vs. θ. Blue, green, and red curves represent energy fractions of the magnetic field (B), proton velocity (V), and proton density (N), respectively. The shaded regions represent standard deviations of $F_{{\rm fast},\epsilon}$ using data sets from $\eta < 10°$ to 30° (binning $\Delta\eta = 1°$). The black dashed curves represent the power-law fits of $F_{{\rm fast},\epsilon}(k_{\perp})$ or linear fit of $F_{{\rm fast},V}(\theta)$.

anisotropy above the CD truncation scales. Below the CD truncation scales, the anisotropy of fast modes enhances as wavenumbers increase. These observations provide the first observational evidence for damping affecting the small-amplitude compressible MHD turbulence cascade on smaller scales within the MHD regime.

(2) Due to the strong dependence on wave propagation angle, CD increases the slow-mode anisotropy parallel to $\boldsymbol{B}_0$, whereas CD increases the fast-mode anisotropy perpendicular to $\boldsymbol{B}_0$.

(3) Fast-mode fractions in the total energy of compressible modes are scale- and angle-dependent and decrease as $k_{\perp}$ (or θ) increases.

These observational results are consistent with theoretical expectations (Yan & Lazarian 2004, 2008). Because the plasma parameters in the analyzed event are common in astrophysical and space plasma systems, our results improve the general understanding of the role of CD in the cascade of compressible turbulence and the corresponding energy transfer, particle transport, and particle energization.

Acknowledgments

We would like to thank the members of the Cluster spacecraft team and NASA's Coordinated Data Analysis Web. The Cluster data are available at https://cdaweb.gsfc.nasa.gov. Data analysis was performed using the IRFU-MATLAB analysis package available at https://github.com/irfu/irfu-matlab. K.H.Y. acknowledges the support from the Laboratory Directed Research and Development program of Los Alamos National Laboratory under project No. 20220700PRD1.

Appendix A
Details of Examination of the Turbulence State

To examine the turbulent state, we calculate the normalized correlation function $R(\tau)/R(0)$, where the correlation function is defined as $R(\tau) = \langle \delta B(t)\delta B(t+\tau)\rangle$, τ is the timescale, and angular

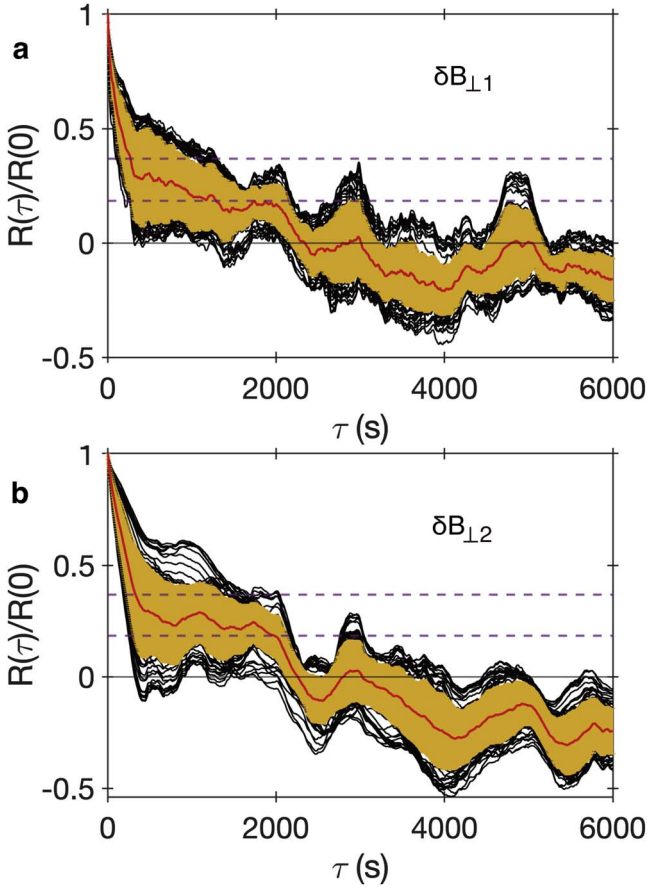

Figure 6. Normalized correlation functions $R(\tau)/R(0)$ vs. τ for $\delta B_{\perp 1}$ and $\delta B_{\perp 2}$ in field-aligned coordinates. The black curves represent $R(\tau)/R(0)$ in all time windows. The red curves represent average values (s) of $R(\tau)/R(0)$ over all time windows. The yellow shaded regions represent $[s-\sigma, s+\sigma]$, where σ represents standard deviations of $R(\tau)/R(0)$. The purple horizontal dashed lines represent $R(\tau)/R(0) = 1/e$ and $1/(2e)$.

brackets represent a time average over the time window length (5 hr). Figure 6 shows $R(\tau)/R(0)$ for magnetic field $\delta B_{\perp 1}$ and $\delta B_{\perp 2}$ components in field-aligned coordinates. Fluctuations $\delta B_{\perp 1}$ are in the $(\hat{\boldsymbol{b}}_0 \times \hat{\boldsymbol{X}}_{\rm GSE}) \times \hat{\boldsymbol{b}}_0$ directions, and $\delta B_{\perp 2}$ are in the $\hat{\boldsymbol{b}}_0 \times \hat{\boldsymbol{X}}_{\rm GSE}$ directions, where $\hat{\boldsymbol{X}}_{\rm GSE}$ is the unit vector toward the Sun from the Earth.

The correlation time is estimated as $T_c \sim \int_0^{R(\tau)\to\frac{1}{2e}} R(\tau)/R(0)d\tau \sim [1300, 2300]$ s. Thus, T_c is much less than the time window length (5 hr), suggesting that the fluctuations are approximately stationary. Moreover, the $R(\tau)/R(0)$ profiles in all time windows are similar, suggesting that the starting time of the moving time window has a slight influence on $R(\tau)/R(0)$, and thus the fluctuations are homogeneous. Above all, it is reasonable to describe structures of turbulent fluctuations using 3D energy distributions.

Appendix B
Schematics of MHD Mode Decomposition and Definition of Symbols

In order to express more clearly and make it easier to understand, we present schematics of MHD mode decomposition in Figure 7 and summarize all symbols in Table 2.

Table 2
The Definition of Symbols

Symbol	Definition
$\boldsymbol{B}_0$	Background magnetic field
δB	rms magnetic field fluctuations
$\delta B_{k,\pm}$	Magnetic field fluctuations of fast (slow) modes
$\delta B_{\rm obs,inplane}$	Magnetic field fluctuations within $\hat{k}\hat{b}_0$ plane observed by FGM
N_0	Background proton density
$\delta N_{k,\pm}$	Proton density fluctuations of fast (slow) modes
$\delta N_{\rm obs}$	Proton density fluctuations observed by CIS-HIA
$V_{\rm A}$	Alfvén velocity
V_S	Sound velocity
V_{Te}	Electron thermal speed
$V_{ph,\pm}$	Phase velocity of fast (slow) modes
δV	rms proton velocity fluctuations
$\delta V_{k,\pm}$	Proton velocity fluctuations of fast (slow) modes
$M_{\rm A,turb}$	Turbulent Alfvén Mach number
β_p	Ratio of proton thermal to magnetic pressure
$d_{\rm sc}$	Spacecraft relative separation
d_i	Proton inertial length
$k_\perp$	Wavenumber perpendicular to background magnetic field
$k_\parallel$	Wavenumber parallel to background magnetic field
$\hat{\boldsymbol{k}}_{\rm SVD}$	Wavenumber direction determined by SVD
$\boldsymbol{k}$ $(\boldsymbol{k}_{Bl})$	Wavevector determined by multispacecraft timing analysis
$\boldsymbol{\xi}_\pm$	Fast- and slow-mode displacement vector
$f_{\rm sc}$	Frequency in the spacecraft frame
$f_{\rm rest}$	Frequency in the plasma flow frame
$\gamma_{\rm fast}$, $\gamma_{\rm slow}$	Fast- and slow-mode damping rate
$\tau_{\rm fast}$, $\tau_{\rm slow}$	Fast- and slow-mode cascading rate
$R_\pm$	Anisotropy of fast and slow modes
θ	Angle between wavevector and background magnetic field
η	Angle between wavevector and $\hat{k}\hat{b}_0$ plane
ζ	Angle between background magnetic field and displacement vector
ϕ	Phase angle of fluctuations in Fourier space
$W_{\epsilon l}$ $(\epsilon \equiv V, B, N)$	Wavelet coefficients of fluctuations
$P_{\epsilon l}$	Power of fluctuations
$D_{\epsilon l}$	Energy density of fluctuations
$D_{B,\rm obs,inplane}$, $D_{N,\rm obs}$	Directly measured energy density of in-plane magnetic field and proton density
$F_{{\rm fast},\epsilon}$	Fast-mode energy to total energy of compressible modes

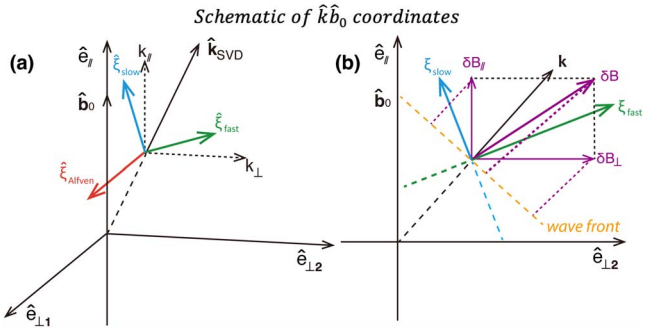

Figure 7. (a) Schematic of $\hat{k}\hat{b}_0$ coordinates determined by $\hat{\boldsymbol{k}}_{\rm SVD}$ and $\hat{\boldsymbol{b}}_0$. The red, blue, and green arrows represent the unit displacement vectors of Alfvén, slow, and fast modes ($\hat{\boldsymbol{\xi}}$, $\hat{\boldsymbol{\xi}}_{\rm slow}$, and $\hat{\boldsymbol{\xi}}_{\rm fast}$). (b) The composition of magnetic field fluctuations (purple arrows). The yellow dashed line marks the wave front.

Appendix C
Examination of the Effects of Angle η

Figure 8 shows wavenumber distributions of proton velocity energy density from three representative data sets ($\eta < 10°$, 20°, and 30°). In general, the main properties of the energy spectra of the slow and fast modes do not significantly change with the increase of η. We note that the anisotropic signature of fast modes is more prominent when we relax the constraints on η. It may be because the mode decomposition between slow and fast modes becomes more incomplete when using a more relaxed η constraint. The η effects on energy distributions are also shown in the shaded regions of Figure 5.

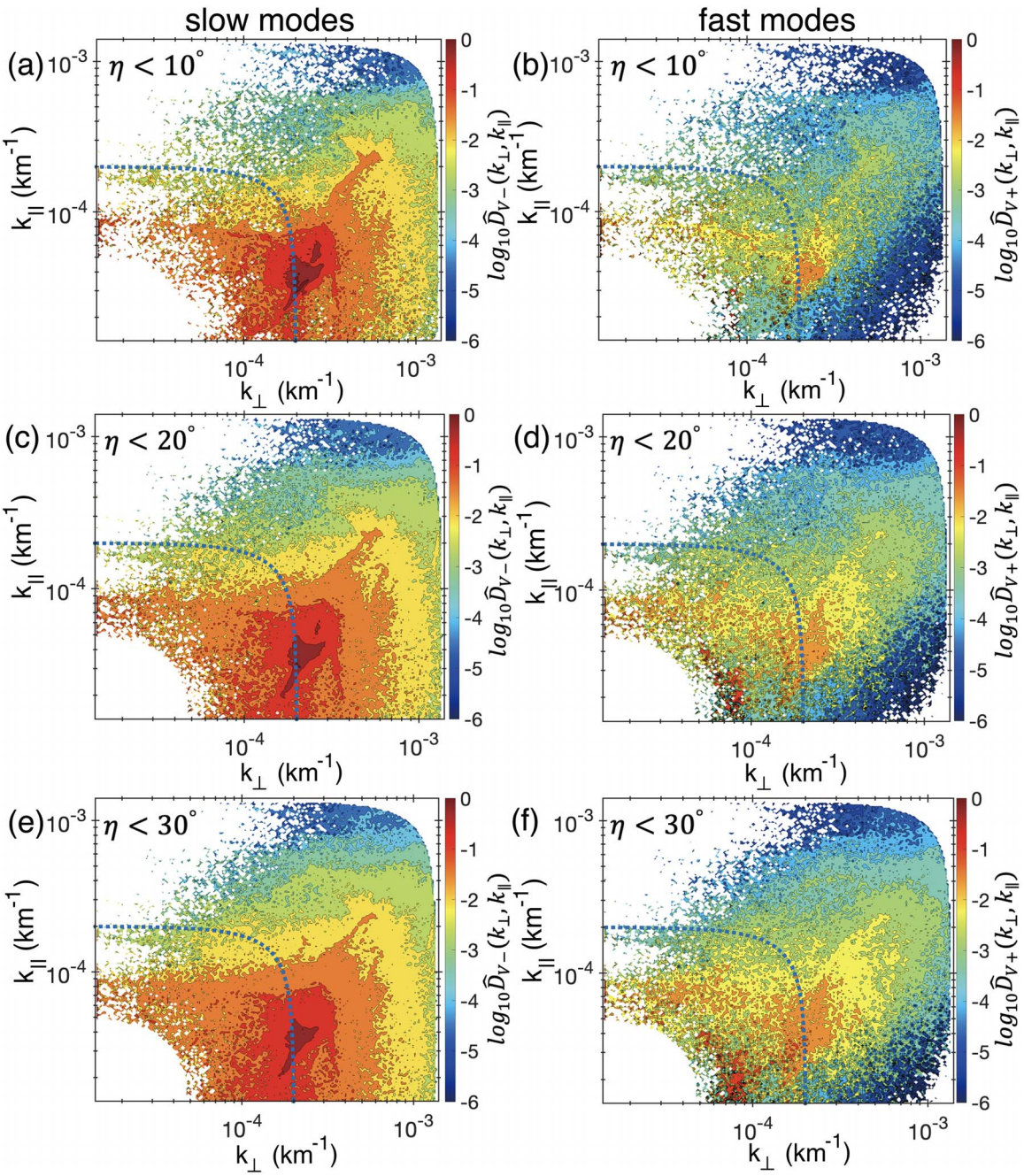

Figure 8. Wavenumber distributions of proton velocity fluctuations under $\eta < 10°$ ((a) and (b)), 20° ((c) and (d)), and 30° ((e) and (f)). (a), (c), and (e) Slow-mode spectra. (b), (d), and (f) Fast-mode spectra. All spectra are normalized with the maximum energy density to facilitate comparison, where $\hat{D}_{c\pm}$ less than 6 orders of magnitude or at $k < 1/(100d_{sc}) = 5 \times 10^{-5}$ km^{-1} is set to zero. The blue dotted curve in each panel marks an isotropic contour at $k = 2 \times 10^{-4}$ km^{-1} as a reference.

Appendix D
Examination of MHD-mode Decomposition

To examine the reliability of MHD-mode decomposition, we compare decomposed magnetic field and density fluctuations (inferred from proton velocity fluctuations using Equations (4) and (5)) with those directly measured by the FGM and CIS-HIA instruments. According to the linearized induction equation, the magnetic field within the $\hat{k}\hat{b}_0$ plane fluctuates along the wave front $\boldsymbol{e}_{wf} = \hat{\boldsymbol{k}} \times (\hat{\boldsymbol{e}}_{\parallel} \times \hat{\boldsymbol{k}})$ (the yellow dashed line in Figure 7(b)). The strength of the magnetic field

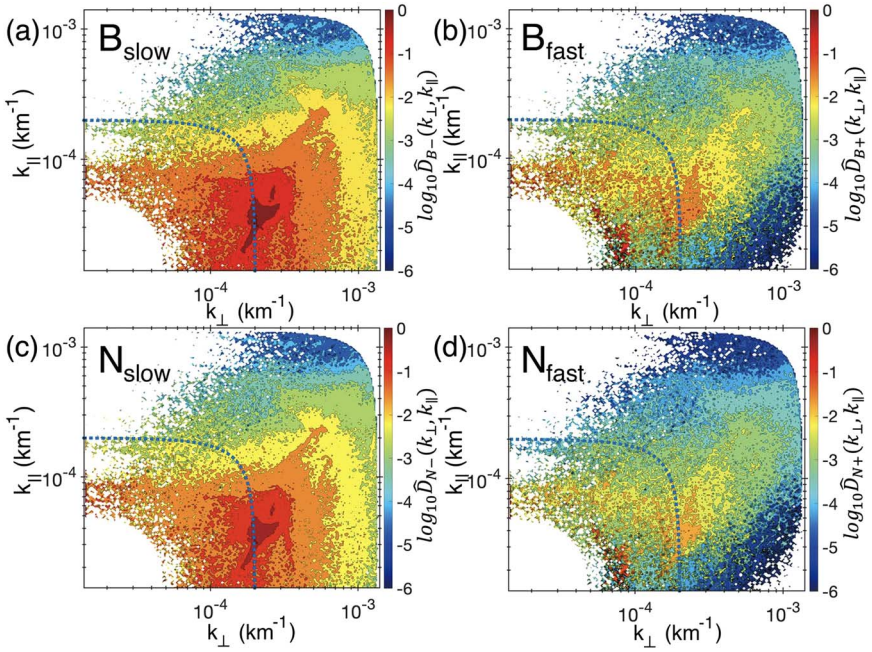

Figure 9. (a) and (b) Wavenumber distributions of slow- and fast-mode magnetic field energy ($\hat{D}_{B-}$ and $\hat{D}_{B+}$), which are normalized with the same constant. (c) and (d) Wavenumber distributions of slow- and fast-mode proton density energy ($\hat{D}_{N-}$ and $\hat{D}_{N+}$), which are normalized with the same constant. $\hat{D}_{\epsilon\pm}$ less than 6 orders of magnitude or at $k < 1/(100d_{sc}) = 5 \times 10^{-5}$ km^{-1} is set to zero. The blue dotted curve in each panel marks an isotropic contour at $k = 2 \times 10^{-4}$ km^{-1} as a reference. These figures use data under $\eta < 20°$.

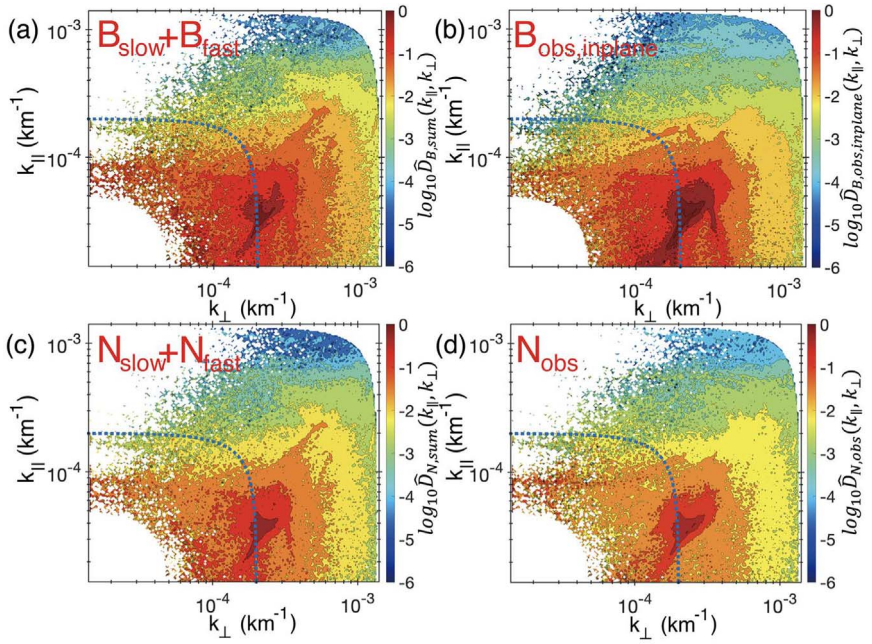

Figure 10. Comparisons of decomposed and directly measured results. (a) and (c) Wavenumber distributions of magnetic field energy within the $\hat{k}\hat{b}_0$ plane ($\hat{D}_{B,\mathrm{sum}}$) and proton density energy ($\hat{D}_{N,\mathrm{sum}}$) inferred from proton velocity energy. (b) and (d) Directly measured wavenumber distributions of magnetic field energy within the $\hat{k}\hat{b}_0$ plane ($\hat{D}_{B,\mathrm{obs,inplane}}$) and proton density energy ($\hat{D}_{N,\mathrm{obs}}$). To reduce the effects of residual energy, spectrum (b) is normalized m times the constant compared to (a), where $m = \langle M_{\mathrm{A,turb}}/(\delta B/B_0)\rangle^2$. Spectra (c) and (d) are normalized with the same constant. The energy density less than 6 orders of magnitude or at $k < 1/(100d_{sc}) = 5 \times 10^{-5}$ km^{-1} is set to zero. The blue dotted curve in each panel marks an isotropic contour at $k = 2 \times 10^{-4}$ km^{-1} as a reference. These figures use data sets under $\eta < 20°$.

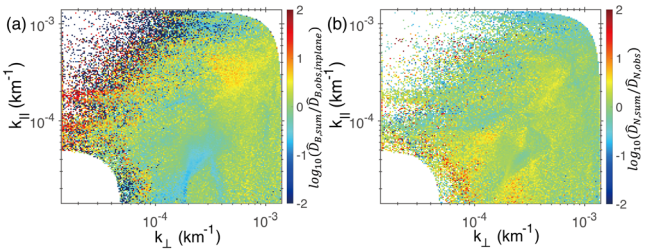

Figure 11. Spectral ratios of decomposed and directly measured results. (a) $\frac{\hat{D}_{B,\mathrm{sum}}}{\hat{D}_{B,\mathrm{obs,inplane}}}$ (the ratio of Figure 10(a) to Figure 10(b)). (b) $\frac{\hat{D}_{N,\mathrm{sum}}}{\hat{D}_{N,\mathrm{obs}}}$ (the ratio of Figure 10(c) to Figure 10(d)). The ratios at $k < 1/(100d_{\mathrm{sc}}) = 5 \times 10^{-5}$ km^{-1} are set to zero. These figures use data sets under $\eta < 20°$.

fluctuations within the $\hat{k}\hat{b}_0$ plane is directly measured by the FGM instruments:

$$|\delta \boldsymbol{B}_{\mathrm{obs,inplane}}| = \langle |\delta B_{k,\parallel}\hat{\boldsymbol{e}}_{\parallel} \cdot \boldsymbol{e}_{wf} + \delta B_{k,\perp 2}\hat{\boldsymbol{e}}_{\perp 2} \cdot \boldsymbol{e}_{wf}| \rangle. \quad \text{(C1)}$$

In wavevector space,

$$\delta B_{k,\parallel} = \sqrt{\sum_{f_{\mathrm{sc}}} D_{B_{\parallel}}(\boldsymbol{k}, f_{\mathrm{sc}}, t)} \exp(2\pi i \phi_1(\boldsymbol{k}, f_{\mathrm{sc}}, t)), \quad \text{(C2)}$$

$$\delta B_{k,\perp 2} = \sqrt{\sum_{f_{\mathrm{sc}}} D_{B_{\perp 2}}(\boldsymbol{k}, f_{\mathrm{sc}}, t)} \exp(2\pi i \phi_2(\boldsymbol{k}, f_{\mathrm{sc}}, t)). \quad \text{(C3)}$$

Similar to Equation (2), we take ϕ_1 and ϕ_2 to be uniform in [0, 2π], and Equation (C1) would be simplified to

$$|\delta \boldsymbol{B}_{\mathrm{obs,inplane}}| \propto |\sqrt{D_{B_{\parallel}}(\boldsymbol{k})}\hat{\boldsymbol{e}}_{\parallel} \cdot \boldsymbol{e}_{wf} + \sqrt{D_{B_{\perp 2}}(\boldsymbol{k})}\hat{\boldsymbol{e}}_{\perp 2} \cdot \boldsymbol{e}_{wf}|. \quad \text{(C4)}$$

The directly observed magnetic field energy within the $\hat{k}\hat{b}_0$ plane is calculated by $D_{B,\mathrm{obs,inplane}} = |\delta \boldsymbol{B}_{\mathrm{obs,inplane}}|^2$. It is worth noting that we have filtered out Alfvén-mode fluctuations (fluctuations out of the $\hat{k}\hat{b}_0$ plane) in this process. On the other hand, magnetic field fluctuations within the $\hat{k}\hat{b}_0$ plane are composed of slow and fast modes, which are inferred from proton velocity fluctuations using Equation (4) (Cho & Lazarian 2003). Figures 9(a) and (b) show wavenumber distributions of slow- and fast-mode magnetic field energy (D_{B-} and D_{B+}). In Figures 10(a) and (b), the total magnetic field energies of the slow and fast modes ($D_{B,\mathrm{sum}} = D_{B+} + D_{B-}$) are roughly consistent with $D_{B,\mathrm{obs,inplane}}$.

Different from magnetic field fluctuations, the proton density fluctuates along wavevectors; thus, all density fluctuations are within the $\hat{k}\hat{b}_0$ plane. The proton density energy directly observed by the CIS-HIA instruments is given by $D_{N,\mathrm{obs}} = \delta N^2_{\mathrm{obs}} \propto \delta N^2_k$. Moreover, based on the continuity equation (Equation (5)), slow and fast modes provide proton density fluctuations together, shown in Figures 9(c) and (d). In Figures 10(c) and (d), the total proton density energies of the slow and fast modes ($D_{N,\mathrm{sum}} = D_{N+} + D_{N-}$) agree well with $D_{N,\mathrm{obs}}$.

Figures 11(a) and (b) show 2D spectral ratios $\frac{\hat{D}_{B,\mathrm{sum}}}{\hat{D}_{B,\mathrm{obs,inplane}}}$ and $\frac{\hat{D}_{N,\mathrm{sum}}}{\hat{D}_{N,\mathrm{obs}}}$, respectively. Most ratios are around unity, suggesting that the results of MHD-mode decomposition are reliable. Moreover, 2D spectral ratios calculated by data sets from $\eta < 10°$ to 30° (binning $\Delta\eta = 1°$) show similar results (not shown).

ORCID iDs

Siqi Zhao https://orcid.org/0000-0003-4268-7763
Huirong Yan https://orcid.org/0000-0003-2560-8066
Terry Z. Liu https://orcid.org/0000-0003-1778-4289
Ka Ho Yuen https://orcid.org/0000-0003-1683-9153
Mijie Shi https://orcid.org/0000-0002-9201-5896

References

Alexandrova, O., Saur, J., Lacombe, C., et al. 2009, PhRvL, 103, 165003
Andrés, N., Sahraoui, F., Galtier, S., et al. 2018, JPlPh, 84, 905840404
Andrés, N., Sahraoui, F., Huang, S., Hadid, L. Z., & Galtier, S. 2022, A&A, 661, A116
Balogh, A., Dunlop, M. W., Cowley, S. W. H., et al. 1997, SSRv, 79, 65
Barnes, A. 1966, PhFl, 9, 1483
Barnes, A. 1967, PhFl, 10, 2427
Brodiano, M., Andrés, N., & Dmitruk, P. 2021, ApJ, 922, 240
Bruno, R., & Carbone, V. 2013, LRSP, 10, 2
Chaston, C. C., Bonnell, J. W., Bale, S. D., et al. 2020, ApJS, 246, 71
Cho, J., & Lazarian, A. 2003, MNRAS, 345, 325
Cho, J., & Lazarian, A. 2005, ThCFD, 19, 127
Cho, J., & Vishniac, E. T. 2000, ApJ, 539, 273
Décréau, P. M. E., Fergeau, P., Krannosels'kikh, V., et al. 1997, SSRv, 79, 157
Galtier, S. 2023, JPlPh, 89, 905890205
Glassmeier, K., Motschmann, U., & Stein, R. 1995, AnGeo, 13, 76
Goldreich, P., & Sridhar, S. 1995, ApJ, 438, 763
Grinsted, A., Moore, J. C., & Jevrejeva, S. 2004, NPGeo, 11, 561
Hollweg, J. V. 1975, RvGeo, 13, 263
Horbury, T. S., Forman, M., & Oughton, S. 2008, PhRvL, 101, 175005
Huang, S. Y., Hadid, L. Z., Sahraoui, F., Yuan, Z. G., & Deng, X. H. 2017, ApJL, 836, L10
Iroshnikov, P. 1963, AZh, 40, 742
Jiang, B., Li, C., Yang, Y., et al. 2023, JFM, 974, A20
Johnstone, A. D., Alsop, C., Burge, S., et al. 1997, SSRv, 79, 351
Kraichnan, R. H. 1965, PhFl, 8, 1385
Leamon, R. J., Smith, C. W., Ness, N. F., & Wong, H. K. 1999, JGR, 104, 22331
Leamon, R. J., Smith, C. W., Ness, N. F., et al. 1998, JGR, 103, 4775
Lithwick, Y., & Goldreich, P. 2001, ApJ, 562, 279
Makwana, K. D., & Yan, H. 2020, PhRvX, 10, 031021
Malik, S., Yuen, K. H., & Yan, H. 2023, MNRAS, 524, 6102
Matthaeus, W. H., Goldstein, M. L., & Lantz, S. R. 1986, PhFl, 29, 1504
Ng, C. S., & Bhattacharjee, A. 1996, ApJ, 465, 845
Oraevsky, V. N. 1983, in Basic Plasma Physics: Selected Chapters, Handbook of Plasma Physics, ed. A. A. Galeev & R. N. Sudan, Vols.1 & 2 (Amsterdam: North-Holland), 75
Oughton, S., Matthaeus, W. H., Wan, M., et al. 2015, RSPTA, 373, 20140152
Petrosian, V., Yan, H., & Lazarian, A. 2006, ApJ, 644, 603
Pincon, J.-L., & Glassmeier, K.-H. 2008, in Multi-Spacecraft Analysis Methods Revisited, ed. G. Paschmann & P. W. Daly (Berlin: Springer), 47
Rème, H., Aoustin, C., Bosqued, J. M., et al. 2001, AnGeo, 19, 1303
Sahraoui, F., Goldstein, M. L., Robert, P., et al. 2009, PhRvL, 102, 231102
Santolík, O., Parrot, M., & Lefeuvre, F. 2003, RaSc, 38, 1010
Stawarz, J. E., Smith, C. W., Vasquez, B. J., Forman, M. A., & MacBride, B. T. 2009, ApJ, 697, 1119
Suzuki, T. K., Yan, H., Lazarian, A., et al. 2006, ApJ, 640, 1005
Taylor, G. I. 1938, RSPSA, 164, 476
Yan, H. 2022, 37th Int. Cosmic Ray Conf., ICRC2021 (Trieste: SISSA), 38
Yan, H., & Lazarian, A. 2002, PhRvL, 89, 281102
Yan, H., & Lazarian, A. 2004, ApJ, 614, 757
Yan, H., & Lazarian, A. 2008, ApJ, 673, 942
Yan, H., Lazarian, A., & Draine, B. T. 2004, ApJ, 616, 895
Yuen, K. H., Li, H., & Yan, H. 2023, NatCo, submitted (arXiv:2310.03806)
Yuen, K. H., Yan, H., & Lazarian, A. 2023, MNRAS, 521, 530
Zank, G. P., & Matthaeus, W. H. 1992, JGR, 97, 17189
Zank, G. P., & Matthaeus, W. H. 1993, PhFl, 5, 257
Zhang, H., Chepurnov, A., Yan, H., et al. 2020, NatAs, 4, 1001
Zhao, S., Yan, H., Liu, T. Z., et al. 2023, NatAs, in press (arXiv:2301.06709v2)
Zhao, S. Q., Yan, H., Liu, T. Z., et al. 2021, ApJ, 923, 253
Zhao, S. Q., Yan, H., Liu, T. Z., et al. 2022, ApJ, 937, 102
Zhu, X., He, J., Verscharen, D., et al. 2020, ApJL, 901, L3